Electronic Journal of Structural Engineering

Original Article

Cite this: DOI:10.56748/ejse.26842

Received Date: 27 June 2025
Accepted Date: 22 January 2026

1443-9255
https://ejsei.com/ejse

Bond-slip performance between welded H-shaped steel and high-performance steel fiber-reinforced concrete based on push-out test

Jianwen ZHANG [a*], Yin ZHANG [a], Gang CHEN [a], Jiansong YUAN [a]

[a] College of Civil Engineering, Henan University of Engineering, Zhengzhou, China
*Corresponding author: 511017988@qq.com

Abstract

Based on the push-out test, the bond-slip behavior between welded H-shaped steel and high-performance steel fiber- reinforced concrete (HPSFRC) was investigated. Four influencing factors including concrete strength, concrete cover thickness, anchorage length and stirrup ratio were considered. Nine specimens were designed according to the orthogonal test design method. The specimens underwent two failure modes: splitting failure and push-out failure. The equivalent constraint coefficient r_e was proposed to determine the failure mode. The average bonding stress slip curves were plotted based on the measured load values and loading end slip data. The expression of multi-factor characteristic bonding strength was fitted. Verification analysis confirmed that the calculated values were in good agreement with the measured values. The ultimate bond strength increased with higher steel fiber volume percentage and concrete cover thickness but decreased as the anchorage length was extended. Stirrups contributed to the enhancement of ultimate bonding strength, yet further increasing the stirrup ratio provided little additional improvement in this strength. Bond-slip constitutive relationships for splitting and push-out failure were developed, with the former adopting a three-stage model and the latter a four-stage model. The slope of the ascending curve of the push-out failure model was slightly larger than that of the splitting failure model, while the descending curve of the splitting failure model was steeper than that of push-out failure model which showed obvious ductile failure characteristics.

Keywords

Welded H-shaped steel, High-performance concrete, Steel fiber, Push-out test, Bond strength, Bond-slip constitutive relationship

1. Introduction

High-performance fiber reinforced concrete (HPFRC) is a type of high-performance concrete that incorporates fiber materials, significantly enhancing its mechanical properties, durability, and other aspects (Kim et al., 2011; Voo and Foster, 2010). It is widely used in the civil engineering field. The fiber types commonly used in HPFRC include the following: steel fiber, carbon fiber, glass fiber, synthetic fiber, and plant fiber (Ming et al., 2021). The steel fibers evenly distributed in the concrete can withstand tensile stress, prevent the expansion of cracks, and make the concrete exhibit better ductility and toughness under load with compressive strength even reaching 200MPa. Research by relevant scholars has demonstrated that High-performance fiber reinforced concrete (HPSFRC) elements possess excellent mechanical properties (Zhang et al., 2023; Wang et al., 2025). HPSFRC composite structures combine the advantages both HPSFRC and composite structures, and have significant application advantages and prospects in high-rise buildings, long-span bridges, dams, underground projects, impact-resistant structures, etc.

The bond-slip performance is the basic mechanical property of concrete structures. Due to the excellent performance demonstrated by steel fiber-reinforced concrete (SFRC) in structures (Tűrker et al., 2021; Yavas and Ince, 2021), a large number of experiments and theoretical studies have been carried out on the bond-slip performance between steel bars and SFRC. The specimens in the study by Shi et al experienced two destruction modes: splitting failure and bar pull-out failure (Shi et al., 2021). Anchorage length was identified as the primary factor influencing bond performance. The anchorage lengths of the specimens were 2d, 4d, and 6d in the experiment. The minimum compressive cubic strength of the concrete was 98.4MPa and the maximum was 126.8MPa. All the specimens in Reference (Wang and Ma, 2018) underwent steel bar pull-out failure. The anchorage lengths of the specimens were 4d, 5d, and 6d, and the concrete strengths grade were C150 and C180. The research results indicated that the presence of steel fibers significantly improved the bonding performance, and the concrete strength had little effect on the bond strength. The research of Hunan University of Technology (Jiang et al., 2022) proposed the bond-slip constitutive relationship between steel bars and HPSFRC. The specimens underwent two failure modes: splitting failure and pull-out failure, and the concrete strength grade was C150. The bond stress and slip curves were simplified into a four-stage linear bonding slip model. The ascending and strengthening sections of the model were in good agreement with the experimental curves, while there were significant errors in the descending and residual sections. Hebei University of Technology (Li et al., 2023) conducted an analysis of the bonding performance and reliability between high-strength steel bars and HPSFRC concrete. The literature proposed the formula of ultimate bonding strength and the design value of critical anchorage length, suggesting that the volume percentage of steel fibers had a significant influence on the bonding strength. Southwest Jiaotong University (Zhao et al., 2019) conducted an experimental study on the bonding performance between steel bars and coarse aggregate ultra-high-performance concrete. The strength of the concrete was 177MPa, and the specimens experienced splitting failure and pull-out failure. The author believed that the anchorage length and the concrete cover thickness had a mutual influence on the bonding performance, and they suggested the minimum concrete cover thickness and the anchorage length. Reference (Yu et al., 2022) conducted experimental research on the bonding performance between HPC and steel bars of different strength grades. It was believed that with the increase of anchorage length, the average ultimate bonding stress increased. With the increase of the ratio of anchorage length to steel bar diameter, the failure mode of the specimens changed from pull-out failure to steel bar tensile failure. Reference (Liang and Huang, 2024) studied the bond strength between steel bars and concrete UHPC by using the beam test method. The research showed that there was a significant linear relationship between the bonding strength and the fiber content. The volume rate of steel fibers was 1%~4% in the test, and the minimum concrete strength was 98.77MPa and the maximum value was 149.46MPa. The author emphasized that when the additional constraints reached a certain limit, the improvement of the bonding strength by further increasing the stirrups was no longer obvious.

As research on SFRC progresses, the use of HPSFRC composite structures is expanding rapidly. (Liu et al., 2023; Zhao et al., 2022). The bond-slip performance of HPSFRC composite structures is an important factor affecting their bearing capacity and deformation. In recent years, some studies on its bond-slip performance have been carried out successively. Reference (Cao et al., 2022) conducted a study on the bond-slip performance between high-strength steel pipes and HPSFRC. It was held that as the strength of concrete increased, the bonding strength decreased, and its strength ranged from C120 to C140. Reference (Yazdan et al., 2014) investigated the local bond-slip performance between cold-rolled steel sections and normal concrete (NC) by pull-out tests and finite element calculations and presented the constitutive relationship model of local bond-slip. Reference (Zhang et al., 2023) investigated the bond-slip performance between H-shaped steel and HPSFRC through push-out tests and finite element calculations and presented the expression of characteristic bonding strength. The study showed that the content of steel fibers, the concrete cover thickness, and the anchorage length all had significant influences on the ultimate bonding strength. Based on experimental research, references (Huang et al., 2024; Huang et al., 2021) presented the bond-slip constitutive relationship between H-shaped steel and HPSFRC and compared it with the finite element analysis results. The minimum cubic compressive strength of the concrete used in the test was 94.9MPa, and the maximum compressive strength of the concrete was 163.7MPa. All specimens experienced push-out failure. Xu et al. (Xu et al., 2024) carried out experimental studies on the bond-slip performance between sections steel and NC as well as between section steel and HPSFRC, reporting the expression of characteristic bond strength and its influencing factors. Among the influencing factors, the effects of stirrup ratio, anchorage length, concrete cover thickness, and concrete strength were considered. Zhang et al. (Zhang et al., 2023) studied the bond-slip performance between fly ash concrete and H-shaped steel with a cubic compressive strength of 112MPa, proposed a five-stage bond-slip constitutive relationship model, and believed that the greatest factor affecting the bond strength was the concrete cover thickness.

Based on the above research results, the main factors affecting the bonding performance between HPSFRC and H-shaped steel are concrete strength, concrete cover thickness, anchorage length and stirrup ratio. In the relevant studies, the value of relative anchorage length la /d was mostly greater than 2 in which la is the anchorage length and d is the height of the H-shaped steel section. The range of la/d values was from 2.59 to 4.31 in reference (Zhang et al., 2023); the range of la/d values was from 4 to 8 in reference (Huang et al., 2024); the range of la/d values was from 2 to 3.5 in reference (Xu et al., 2024); the range of la/d values was from 3.4 to 6.4 in reference (Ming et al., 2021) ; the range of la/d values was from 2 to 3.6 in reference (Zhang et al., 2023). With the increase of anchorage length, the effective transfer length of bonding stress relatively decreased, and failure may occur at the loading end. The studies of the push-out tests about literatures (Zhang et al., 2023; Xu et al., 2024; Ming et al., 2022) showed that the bonding stress between section steel and high-performance concrete at the loading end decreased rapidly with the increase of anchorage length, and the local maximum bonding strength at the loading end exceeded 10 MPa. The American scholar Roeder (Roeder et al., 1999) believed that the bonding stress presented a triangular distribution within a length range twice the height of the section steel. Therefore, an excessively long anchorage length was of no significance for improving the bonding bearing capacity. At present, there are no reports on the experimental research on the bonding performance between HPSFRC and section steel with a relative anchorage length less than 2, and there are also few experimental studies on la/d less than 3. The bond failure between HPSFRC and section steel mainly included two types: brittle failure and ductile failure (Ming et al., 2022). Brittle failure occurs abruptly. Specifically, when the maximum bonding strength is attained, the bearing capacity drops sharply accompanied by relatively small corresponding deformation. In contrast, ductile failure is characterized by significant slippage of the specimen either when it reaches the maximum bonding strength or when the bonding strength only experiences a slight reduction. Although the current literature has described the failure types and phenomena of damage but does not provide the criteria for identifying the types of damage. Therefore, it is necessary to carry out experimental research on the bond-slip performance of specimens with the relative anchorage length less than 2 to further study the failure mode, bond strength and bond-slip constitutive relationship.

2. Experimental Program

2.1 Materials

The main components of HPC are sand, Portland cement, silica fume, slag, fly ash, limestone, steel fiber, etc. (Liu et al., 2025) Coarse aggregates were incorporated into HPC with a focus on studying their impacts on the material's workability and deformation performance (Jin et al., 2023). The HPC used in the experiment has three strength grades: C100, C120 and C150. The mixture configuration is shown in Table 1. The cement used is ordinary Portland cement P.O. 52. 5, and ρ_{vf} is the volume percentage of steel fibers. The steel fiber has a length of 13 ± 1.3mm with a length-to-diameter ratio of 65% and a tensile strength of 2850MPa.

First, the mixture consisting of cement, silica fume, quartz sand and slag was stirred thoroughly for 3 minutes. Subsequently, the water-reducing agent and water were incorporated into the mixture, which was then stirred for a period of 3 to 5 minutes to preliminarily form a homogeneous slurry. Finally, the remaining water and steel fibers were divided into several equal portions and added sequentially to the mixture, followed by further stirring for 5 to 10 minutes to ensure uniform dispersion of the steel fibers and satisfactory workability of the concrete. For each concrete strength grade, three cubic specimens with a side length of 100 mm were cast. The mix proportions of the concrete materials and the average cubic compressive strength f_{cu} are shown in Table 1.

Table 1. Mix proportions of HPC

Type	W/B (%)	Cement (Kg/m³)	Water (Kg/m³)	Quartz sand (Kg/m³)	Silica fume (Kg/m³)	Slag (Kg/m³)	Water-reducing agent (Kg/m³)	ρ_{vf} (%)	F_{cu} (MPa)
C100	0.25	875	219	1058	95	150	7.8	1.2	100.5
C120	0.2	972	195	923	150	182	6.2	1.8	127.6
C150	0.2	972	195	923	150	182	6.2	4.2	150.5

The steel bars used in the test were HRB400 hot-rolled steel bars, and the welded H-shaped steel were made of Q335 steel plates. The mechanical properties are shown in Table 2 where f_y represents the yield strength, f_u represents the ultimate strength, and E_s represents the elastic modulus.

Table 2. Mechanical properties of the bar and H-shaped steel

Type	Member	Dimension (mm)	F_y (MPa)	F_u (MPa)	E_S (GPa)
HRB400	Stirrup	6	428.3	537.4	205
HRB400	Longitudinal steel bar	12	417.5	641.3	205
Q335	Flange of the shape	14	562.9	618.5	205
Q335	Web of the shape	14	562.9	618.5	205

2.2 Specimen design and fabrication

Nine specimens were designed using the orthogonal test method taking into account four factors : concrete strength, concrete cover thickness, anchorage length and stirrup ratio. Details of the specimens are shown in Table 3 in which l_a represents the anchorage length, C_{ss} represents the concrete cover thickness of the steel frame, *and* b and h represent the cross-sectional dimensions of the specimens.

The cross-section and longitudinal view of the specimen are shown in Fig.1, where s represents the stirrup spacing.

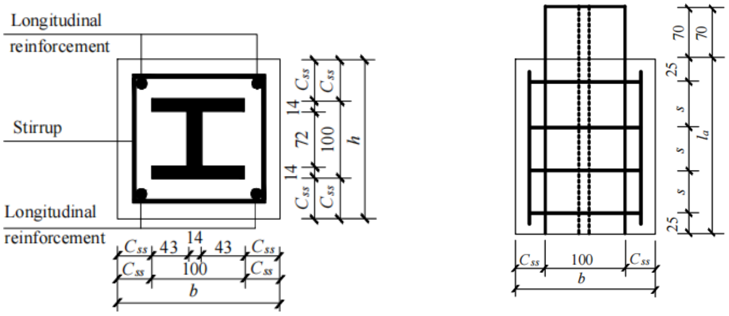

(a) Cross section

(b) Longitudinal view

Fig. 1 Schematic diagram of specimen size

Table 3. Parameters of the specimens

NO.	b/mm	h/mm	f_{cu}/MPa	l_a/mm	C_{ss} / mm	Stirrup (mm)	Stirrup ratio (%)
1-1	180	180	100.5	100	40	Ø6@50	0.63
1-2	220	220	100.5	200	60	Ø6@100	0.26
1-3	260	260	100.5	300	80	0	0
2-1	220	220	127.6	100	60	0	0
2-2	260	260	127.6	200	80	Ø6@50	0.43
2-3	180	180	127.6	300	40	Ø6@100	0.31
3-1	260	260	150.5	100	80	Ø6@100	0.21
3-2	180	180	150.5	200	40	0	0
3-3	220	220	150.5	300	60	Ø6@50	0.51

H-shaped steel was welded from steel plates with 14mm thickness. Prior to fabricating the specimens, the surface of the H-shaped steel was ground to remove welding slag and rust. A positioning symbol was drawn at the center of the bottom of the wooden formwork to ensure that the H-shaped steel was centered in the specimen. The center of the H-shaped steel section should be coincided with the positioning symbol. Concrete was poured vertically along the H-shaped steel, the formwork was struck with a wooden hammer after pouring. When the concrete no longer sank and the surface of the specimen showed slurry, it indicated that the concrete had become compact and the internal air had basically been expelled. After the specimen was made, it was placed in the laboratory to naturally solidify for one day. On the following day, the specimens were demolded and then placed in a standard curing room for a 28-day curing period.

2.3 Loading scheme

The test loading device is shown on Fig.2. The test was carried out on a 100t test machine. The upper part is the loading end, and the lower part is the free end. A steel stool was fabricated with a square hole drilled in its center. To maximize the compressive area of the concrete at the free end, the size of this square hole should be minimized as far as practicable. The side length of the square opening hole is 106mm, and each side is 6mm larger than the size of the H-shaped steel. Owing to such factors as formwork fabrication tolerances, section steel positional deviations during concrete pouring, and non-uniform concrete hardening shrinkage, pre-test measurements were meticulously conducted on the specimen dimensions and concrete cover thickness before the specimens were placed on the testing machine. The specimen positioning line was drawn on the steel stool to ensure the smooth push out of the H-shaped steel at the free end. A preload of 30kN was carried out first to reduce the slip measurement error caused by the gap between the specimen and the loading plate. The loading was carried out by the displacement control method, and the loading speed is 0.1mm/min.

Displacement gauges were installed at both the loading end and the free end of the specimen. The slip measured at the loading end included the compressive deformation of the 70mm H-shaped steel exposed section, which needed to be subtracted from the measured values.

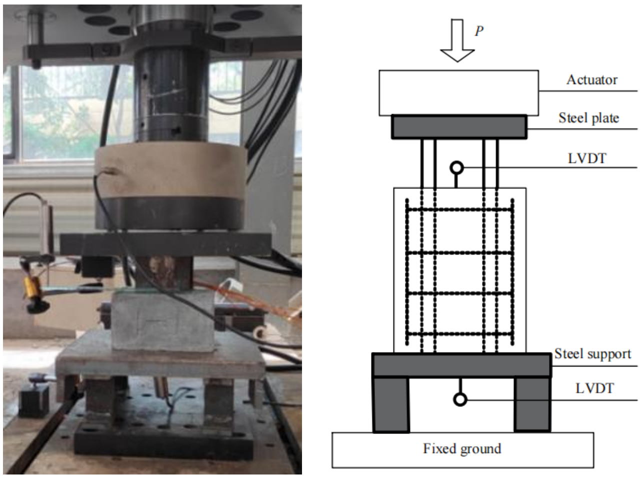

(a) Testing machine (b) Layout of test measuring equipment

Fig. 2 Compressive loading test

3. Test results and analysis

3.1 Failure models

Splitting failure

Specimens 1-1, 1-2, 1-3, 2-1 and 3-1 suffered splitting failure, while specimens 2-2, 2-3, 3-2 and 3-3 suffered push-out failure. Photos of the specimen failure are shown in Fig. 3. The top section of the photo corresponds to the loading end.

Splitting failure occurred when the concrete strength was low and the anchorage length of the specimen was short. When the load was approximately 12% to 30% of the ultimate load, no slippage occurred at the loading end. With increase of the load, the slip gradually increased, and a very small number of tiny cracks occurred at the loading end. During the loading process, a sharp scraping noise was audible between the steel fibers and H-shaped steel, arising from their relative slippage. At the point of ultimate load, a loud "bang" accompanied a sudden sharp drop in load. One or two of the originally fine cracks suddenly penetrated the entire specimen, and a relatively obvious crack appeared on the surface of the column body which ran from top to bottom throughout the entire surface of the specimen. The maximum crack width was approximately 1mm, and the concrete underwent splitting failure. Splitting failure occurs abruptly, which is characterized by a sharp load drop and minimal slip increment and is classified as brittle failure. When the load decreased to a certain level and stabilized thereafter, this load was defined as the residual load, which accounted for approximately 54% to 63% of the ultimate load.

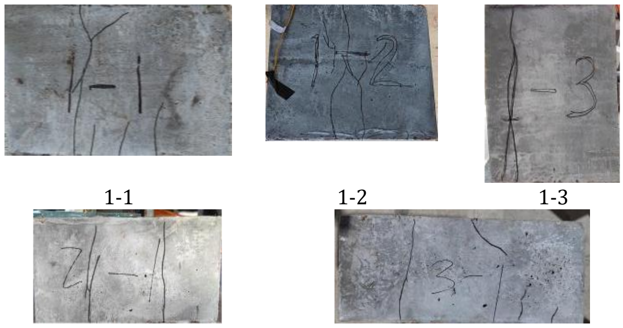

(a) Split failure

(b) Push-out failure

Fig. 3 Specimen failure photos

Push-out failure

For specimens with high concrete strength and long anchorage lengths, push-out failure was observed. When the load was approximately 11% to 28% of the ultimate load, no slippage occurred at the loading end. With the increase of the load, the slip increased almost linearly proportional to the load. The hissing scraping sound caused by the relative sliding between steel fibers and the surface of steel could be clearly heard. When the load exceeded about 80% of the ultimate load, the slip growth rate increased significantly, and very few fine cracks appear at the loading end. Upon reaching the ultimate load, the load either stabilized or decreased gradually, whereas the H-shaped steel was slowly pushed out. The specimen underwent push-out failure and presented the characteristics of ductile failure. Few fine cracks appeared on the side of the column body of specimens 2-3 and 3-2 and no cracks formed from top to bottom. The minimum concrete cover thickness was set at 40 mm, consequently, the cracks generated by bond failure between the H-shaped steel and concrete interface propagated to the specimen surface. The concrete cover thicknesses of specimens 2-2 and 3-3 were 80mm and 60mm respectively, and no cracks occurred in the column bodies.

When the specimen underwent failure, the loading end and free end exhibited two dominant crack forms: diagonal cracks and straight cracks (see Fig. 4). The oblique cracks were approximately at a 45° angle, and the straight cracks were basically parallel to the cross-sectional size direction of the specimen. The cracks shown in the schematic diagrams of Figures 4(a) and 4(b) are in four directions. However, due to manufacturing errors and material non-uniformity, only tiny cracks emerged in one or two directions where the material was relatively weak. When the specimen was damaged, the crack morphology at the end might be either straight cracks or oblique cracks, as shown in the photo of Figure 4(c).

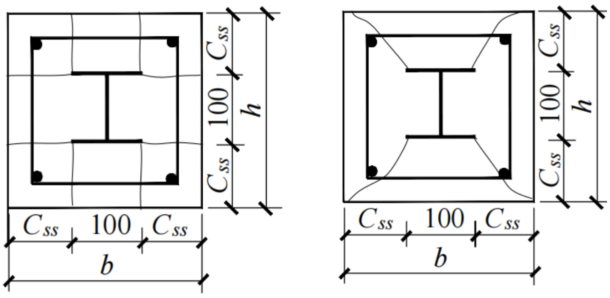

(a) Straight crack (b) Oblique crack

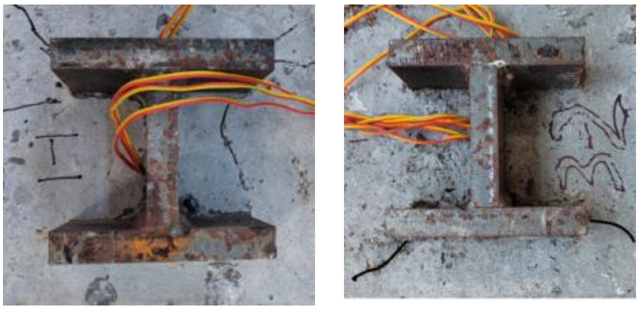

(c) Crack photo

Fig. 4 Crack morphology diagram

Identification of damage mode

Specimens 1-1, 1-2 and 1-3, which had the lowest concrete strength, all suffered splitting failure. Similarly, specimens 2-1 and 3-1 experienced splitting failure due to their shortest anchorage length. Therefore, the main factors influencing the failure mode are the strength of concrete and the anchorage length. The concrete strength exhibited a positive correlation with the steel fiber volume fraction ρ_{vf} in this experiment. Increasing the stirrup ratio ρ_{sv} could enhance the binding effect of stirrups on concrete and improve the strength and ductility of concrete. Therefore, the equivalent constraint coefficient r_e was introduced to determine the type of bonding failure which considered the influences of ρ_{vf}, ρ_{sv} and the relative anchorage length l_a/d. The expression of r_e is shown as Eq. (1).

$$\gamma_e = (\rho_{vf} + \rho_{sv}) \cdot \frac{l_a}{d} \tag{1}$$

Table 4. Equivalent constraint coefficient re

Specimen	1-1	1-2	1-3	2-1	2-2	2-3	3-1	3-2	3-3
r_e （%）	1.83	2.92	3.6	1.8	4.46	6.33	4.41	8.4	14.13
Failure model	S	S	S	S	P	P	S	P	P

The failure mode of the specimens (Huang, et al., 2021) is verified by r_e as shown in Table 5. The predicted failure mode is completely consistent with the test failure mode.

Where d represents the height of the section steel. The calculation results of the equivalent constraint coefficient r_e of the specimen are shown in Table 4, where S represents splitting failure and P represents push-out failure. As the equivalent constraint coefficient increases, splitting failure transforms to push-out failure. The maximum value of r_e for the splitting failure specimens is 4.41%. Taking 4.41% as the critical value, splitting failure occurs when r_e≤4.41%, and push-out failure occurs when r_e>4.41%.

Table 5. Prediction and comparison of failure mode

NO.	ρ_{vf} (%)	ρ_{sv} (%)	$\frac{l_a}{d}$	r_e (%)	Prediction	Test
1	0	0.28	3.57	1	S	S
2	1	0.28	3.571	4.57	P	P
3	2	0.28	3.57	8.14	P	P
4	2	0.23	3.57	7.96	P	P
5	2	0.19	3.57	7.82	P	P
6	2	0.56	3.57	9.14	P	P
7	2	014	3.57	7.64	P	P
8	2	0	3.57	7.14	P	P
9	2	0.28	5.25	12	P	P
10	2	0.28	7.14	16.29	P	P

3.2 Load-slip curve at loading end

When the load was small, there was almost no slippage at the free end. When the load approached or reached the ultimate load, the slip at the free end suddenly increased, but it was relatively smaller compared to the slip at the loaded end. The slip at the loading end exhibited a distinct regularity with increasing load, and the corresponding experimental data demonstrated good stability. Therefore, the load-slip relationship curve at the loading end was selected as the primary focus of the analysis. The load P and the slip S_l curves at the loading end are shown in Fig. 5.

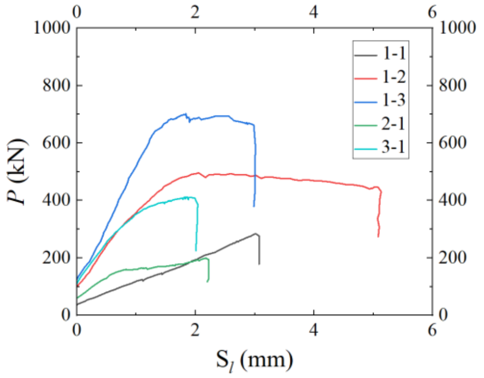

(a) Split failure

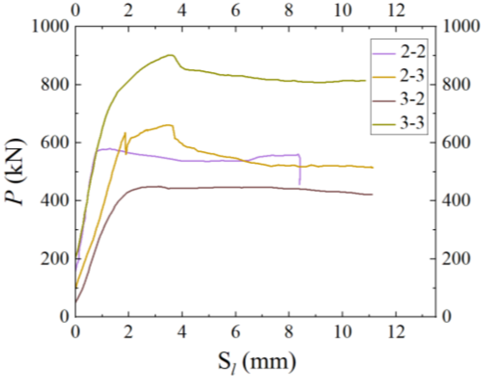

(b) Push-out failure

Fig. 5 P-Sl Curve

Based on the analysis of the measured curves in Fig.5, the relationship models between the load P and the sliding S_l at the loading end for splitting failure and push-out failure are shown in Fig. 6.

The load-slip curve of the splitting failure specimen is divided into three sections: the non-slip section OA, the ascending section AB, and the descending section BC. The chemical bonding force played a major role in the non-sliding section. Once the chemical bonding force was lost, relative slippage initiated at the loading end. At this point, the corresponding load was defined as the initial sliding load P_0, and the frictional force and mechanical locking force began to play a role (the frictional force played a major role) until the ultimate load P_u was reached. The H-shaped steel was subjected to the pressure of the push-out load P longitudinally and underwent expansion deformation laterally. Due to the expansion deformation, lateral compressive stress was generated on the interface concrete. With the increase of load P, the compressive stress became larger and larger. When the tensile stress at the cross-section of the concrete's weak zones exceeded the tensile strength, splitting cracks were initiated in the concrete, as illustrated in Fig.7. Splitting failure was mainly caused by the generation of splitting cracks, resulting in a decrease in bearing capacity. When the anchorage length of the specimen was relatively short, the average bond shear stress at the section steel-concrete interface was comparatively high. Since such shear stress was detrimental to the concrete's tensile strength, splitting failure was thus prone to occur when the concrete strength was low. During the load drop section, the adhesive force provided by the large frictional force at the interface could continue to bear the load due to the presence of steel fibers in the concrete. At this time, the end point of the load drop section was denoted as the residual load P_r. The slips corresponding to the ultimate load P_u and the residual load P_r were defined as the ultimate load slip S_u and the residual slip S_r, respectively.

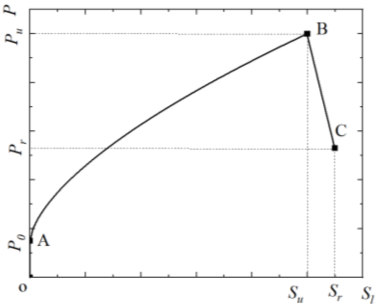

(a) Split failure

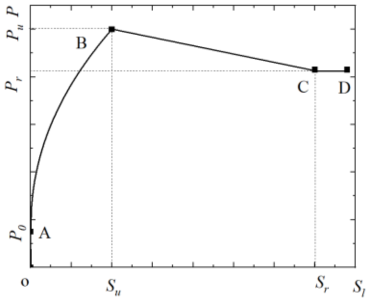

(b) Push-out failure

Fig. 6 P-Sl Curve model

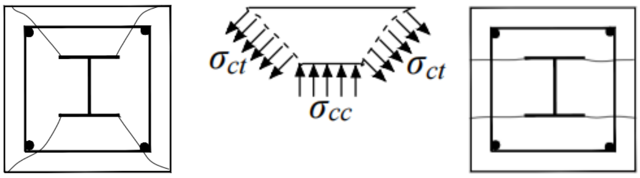

(a) Stress of oblique crack section

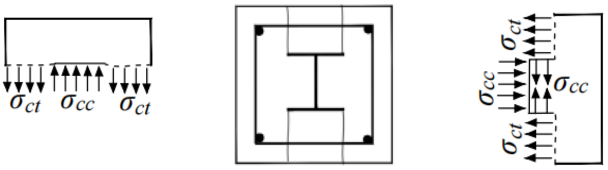

(b) Stress of straight crack section

Fig. 7 Stress of cracked section

The load-slip curve of the push-out failure specimen is divided into four sections: the non-slip section OA, the ascending section AB, the descending section BC and the converging section CD. The bonding mechanisms for the non-slip and ascending stages are the same as those associated with splitting failure. When the ultimate load P_u was reached, the number of cracks at both the loading end and the free end of the specimen was not only smaller than that observed in the splitting failure, but the crack width was also narrower. Some specimens exhibited no cracks whatsoever on their sides. When the anchorage length of the specimen was longer and the average shear stress was lower, this condition was relatively favorable to the tensile strength of the concrete. Concrete with a larger volume percentage of steel fibers has a higher strength, and steel fibers can restrict the development of cracks (Xu et al., 2024). Hence, as the steel fiber content and anchorage length increases, splitting cracks become less likely to form in the specimens. Push-out failure occurred when the shear stress at the interface between H-shaped steel and concrete exceeded the ultimate bonding strength, such as specimens 2-2, 2-3, 3-2 and 3-3. In this test, it was observed that an increase in concrete strength, coupled with a higher volume percentage of steel fibers, led to a greater frictional force at the interface between H-shaped steel and concrete. The continuously increasing slip required constantly overcoming the frictional force on the interface. Therefore, the specimen was capable of sustaining large slippage, with only a slight reduction in bearing capacity that tended to stabilize. The minimum load in the descending section was taken as the residual load P_r which was mainly provided by the friction force. Meanwhile, the slips corresponding to the ultimate load P_u and residual load P_r were designated as the ultimate load slip S_u and the residual slip S_r, respectively.

3.3 Bond strength

Characteristic bonding strength

The average bonding stress τ can be obtained by dividing the load at the loading end by the contact area at the interface between H-shaped steel and concrete. In the Eq. (2), C_a represents the perimeter of the H-shaped steel section. Fig.8 presents the measured curves of the average bonding stress τ and the slip S_l at the loading end of each specimen.

$$\tau = \frac{P}{C_a l_a} \tag{2}$$

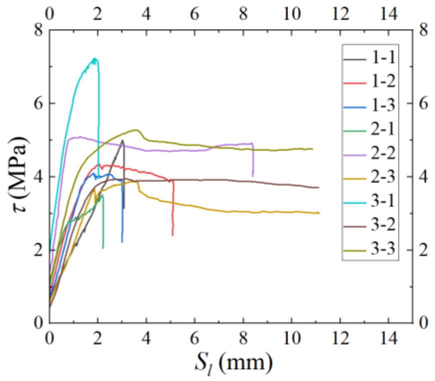

Fig. 8 τ-Sl curve

The characteristic bonding strengths of each specimen can be calculated from the measured characteristic loads as shown in Table 6. τ_0 is the initial slip bonding strength, τ_u is the ultimate bonding strength, and τ_r is the residual bonding strength.

Table 6. Test results of characteristic bond strength

NO.	P_0 (kN)	P_u (kN)	P_r (kN)	S_u (mm)	S_r (mm)	τ_0 (MPa)	τ_u (MPa)	τ_r (MPa)	τ_0/τ_u (%)	τ_r/τ_u (%)
1-1	35	284.7	178.8	3.01	3.07	0.61	4.99	3.14	12.2	62.9
1-2	100	493.5	274	2.05	5.08	0.88	4.33	2.4	20.3	55.4
1-3	124.8	701.8	379	1.84	2.98	0.73	4.1	2.22	17.8	54.1
2-1	60	200.2	117	2.18	2.2	1.05	3.51	2.05	30	58.4
2-2	160	580.5	480	1.29	8.41	1.4	5.09	4.21	27.5	82.7
2-3	98.7	661	514	3.48	11.09	0.58	3.87	3	15	77.5
3-1	110	412.7	225	1.86	2.01	1.93	7.24	3.95	26.7	54.6
3-2	50.5	449.9	422.4	3.09	10.9	0.44	3.95	3.7	11.1	93.7
3-3	206	902	806.6	3.62	9.28	1.2	5.27	4.72	22.8	89.6

The bonding strength between H-shaped steel and HPSFRC is primarily composed of chemical adhesion, frictional resistance, and mechanical interlocking (Huang et al., 2018). As presented in Table 6, the ratio of the initial bonding strength to the ultimate bonding strength exceeds 10%, with a maximum value of 30%. When relative slippage occurred between H-shaped steel and concrete, the chemical bonding force was lost, and the bonding strength was mainly provided by frictional force and mechanical interlocking force, with frictional force contributing the most significantly. Regardless of the form of failure, a certain residual bonding strength was retained at the interface between H-shaped steel and HPSFRC. For specimens failing in splitting, the ratio of residual bond strength to ultimate bond strength exceeded 50%; while for those failing in push-out, this ratio surpassed 75%.

Analysis of Influencing Factors of Bonding Strength

Relevant literature has studied the average bonding strength between section steel and HPSFRC and analyzed the influencing factors and variation laws governing the characteristic bonding strength. In the analysis of characteristic bonding strength in reference (Zhang et al., 2023), the influencing factors related to concrete cover thickness c_{ss}, relative anchorage length l_a/d, volume percentage of steel fibers ρ_{vf} and stirrup ratio ρ_{sv} were taken into consideration. The analysis of the characteristic bonding strength in reference (Zhang et al., 2023) took into account the influences of the relative concrete cover thickness c_{ss}/d, the relative anchorage length l_a/d, and the stirrup ratio ρ_{sv}. In contrast, Reference (Huang et al., 2021) analyzed the characteristic bonding strength by considering the influences of the relative concrete cover thickness c_{ss}/d, the cubic compressive strength of the concrete f_{cu}, and the volume percentage of steel fibers ρ_{vf}. However, the relevant literature only adopted its own experimental results to fit and compare the characteristic bonding strength and failed to verify and analyze these findings using experimental data from other studies. By combining the experimental data from relevant literature with the results of this test, the influences of four key parameters are considered: steel fiber volume percentage ρ_{vf}, relative concrete cover thickness c_{ss}/d, relative anchorage length l_a/d, and stirrup ratio ρ_{sv}. Scatter plots illustrate the relationship between the ultimate bonding strength τ_u and its influencing factors are drawn, as presented in

Fig. 9. The ultimate bonding strength of different specimens with the same factor is taken as the average value.

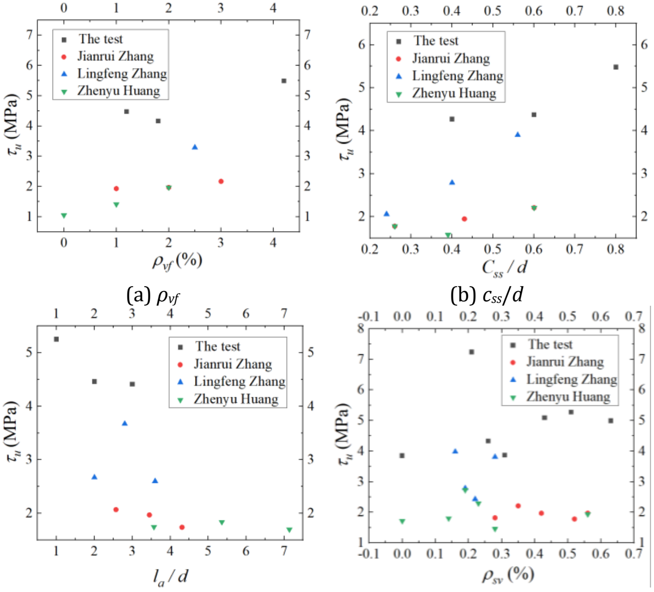

(a) ρ_{vf} (b) c_{ss}/d

(c) l_a/d (d) ρ_{sv}

Fig. 9 Graph of ultimate bonding strength and influencing factors

The combined test results reveal that the ultimate bonding strength rises with increasing ρ_{vf} and c_{ss}/d, but declines with an increase in l_a/d. The bonding strength of the specimens with stirrups is higher than that of the specimens without stirrups. Yet, as the stirrup ratio ρ_{sv} continues to rise, its influence on bond strength becomes less significant. The single factor scatter plots exhibit relatively high data dispersion; therefore, a comprehensive analysis should be conducted to evaluate how these influencing factors affect bond strength. Based on the data of this experiment and related tests, the expression of multi-factor characteristic bond strength is fitted as Eqs. (3), (4) and (5).

$$\tau_0 = -0.83 + 0.08\rho_{vf} + 1.53\frac{c_{ss}}{d} + 0.61\frac{d}{l_a} + 0.97\rho_{sv} \tag{3}$$

$$\tau_u = -1.8 + 0.6\rho_{vf} + 4.34\frac{c_{ss}}{d} + 2.94\frac{d}{l_a} + 1.17\rho_{sv} \tag{4}$$

$$\tau_r = -0.92 + 0.63\rho_{vf} + 2.95\frac{c_{ss}}{d} + 0.72\frac{d}{l_a} + 1.1\rho_{sv} \tag{5}$$

The comparison between the calculated values of the characteristic bonding strength (τ_{0c}、τ_{uc}、τ_{rc}) and the corresponding test values (τ_{0t}、τ_{ut}、τ_r) is shown in Fig.10. The calculated values and the test values exhibit relatively good consistency.

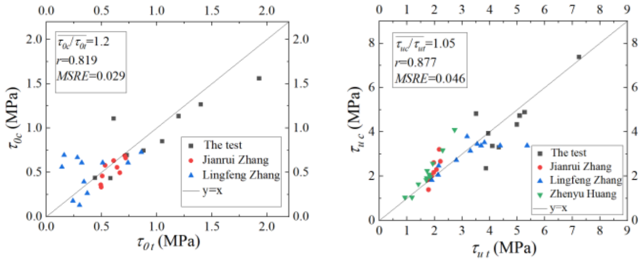

(a) Prediction of τ_0 (b) Prediction of τ_u

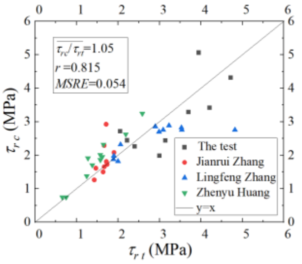

(c) Prediction of τ_r

Fig.10 Comparison of characteristic bonding strength

Accuracy and error analyses of the fitting calculation of the characteristic bonding strength can be derived from further data analysis. In Fig.10, $\overline{\tau_{0c}/\tau_{0t}}$、$\overline{\tau_{uc}/\tau_{ut}}$、$\overline{\tau_{rc}/\tau_{rt}}$ represent the average values of the ratios between the calculated and the experimental values of the characteristic bond strength, *r* denotes the fitting correlation coefficient, and *MSRE* stands for the mean squared relative error. The analysis results indicate that the fitting formula for characteristic bonding strength is in good agreement with the measured values and can provide the predicted value of the characteristic bond strength with relatively high accuracy.

4. Bond stress-slip constitutive relationship

Using the average bond stress at the loading end and measured slip curves, the bond-slip constitutive relationship models for splitting failure and push-out failure can be established respectively. The constitute relation model is shown on Fig.11. The splitting failure model is divided into three stages: the non-slip segment OA, the ascending segment AB and the descending segment BC. In contrast, the push-out failure model comprises four stages, namely the non-slip segment OA, the ascending segment AB, the descending segment BC and the convergent segment CD.

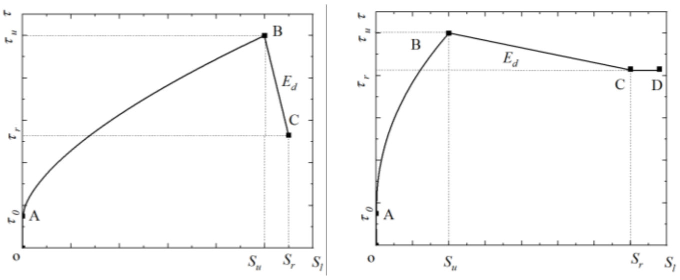

(a) Splitting failure (b) Push-out failure

Fig. 11 τ-s_l constitutive relation model

The expression of constitutive relation model for splitting failure is shown as Eq. (6).

$$\tau = \begin{cases} \tau_0 & (s = 0) \\ = \tau_0 + (\tau_u - \tau_0)\left(\frac{s}{s_u}\right)^{0.63} & (0 \le s \le s_u) \\ = \tau_u + \left(\frac{\tau_r - \tau_u}{s_r - s_u}\right)(s - s_u) = \tau_u + E_d(s - s_u) & (s_u \le s \le s_r) \end{cases} \tag{6}$$

The expression of constitutive relation model for push-out failure is shown as Equation (7).

$$\tau = \begin{cases} = \tau_0 & (s = 0) \\ = \tau_0 + (\tau_u - \tau_0)\left(\frac{s}{s_u}\right)^{0.46} & (0 \le s \le s_u) \\ = \tau_u + \left(\frac{\tau_r - \tau_u}{s_r - s_u}\right)(s - s_u) = \tau_u + E_d(s - s_u) & (s_u \le s \le s_r) \\ = \tau_r & (s \ge s_r) \end{cases} \tag{7}$$

The characteristic bond strengths τ_0, τ_u and τ_r in the bonding stress expressions are calculated respectively by Eqs. (3), (4) and (5). The characteristic slip parameters, namely the peak slip s_u and residual slip s_r were fitted using from data of this experiment. The peak slip s_u for the push-out failure and splitting failure adopts the same Eq. (8). The residual slip of splitting failure s_{rs} and that of push-out failure s_{rp} are calculated using Eqs. (9) and (10), respectively.

$$s_u = 4.47 - 0.19\rho_{vf} - 3.71\frac{c_{ss}}{d} - 0.59\frac{d}{l_a} + 0.54\rho_{sv} \tag{8}$$

$$s_{rs} = 13.9 + 1.13\rho_{vf} - 12\frac{c_{ss}}{d} - 6.9\frac{d}{l_a} \tag{9}$$

$$s_{rp} = 13.9 - 0.16\rho_{vf} - 7.17\frac{c_{ss}}{d} + 1.1\frac{d}{l_a} \tag{10}$$

The comparison between the predict values and the test values for the characteristic bond strength and the characteristic slip is presented in Table 7, where s_{rc} and s_{rt} denote the calculated and measured values of residual slip, respectively; s_{uc} and s_{ut} represent the calculated and measured values of peak slip, respectively; $\triangle\tau$ and $\triangle s$ refer to the differences between the calculated and the experimental values of characteristic bond strength and characteristic slip, respectively.

The fitting of the characteristic bonding strength calculation formula incorporated both the data from this test and relevant research data. The average ratio of the calculated characteristic bonding strength to the measured value exceeded 90%, with the relative error remaining below 20%. It is indicated that the proposed formula was accurate and stable. In contrast, the fitting of the characteristic slip calculation formula was based solely on the data from this test, consequently, the relative value of calculated characteristic slip to the measured value is close to 1, and the relative error is less than 13%.

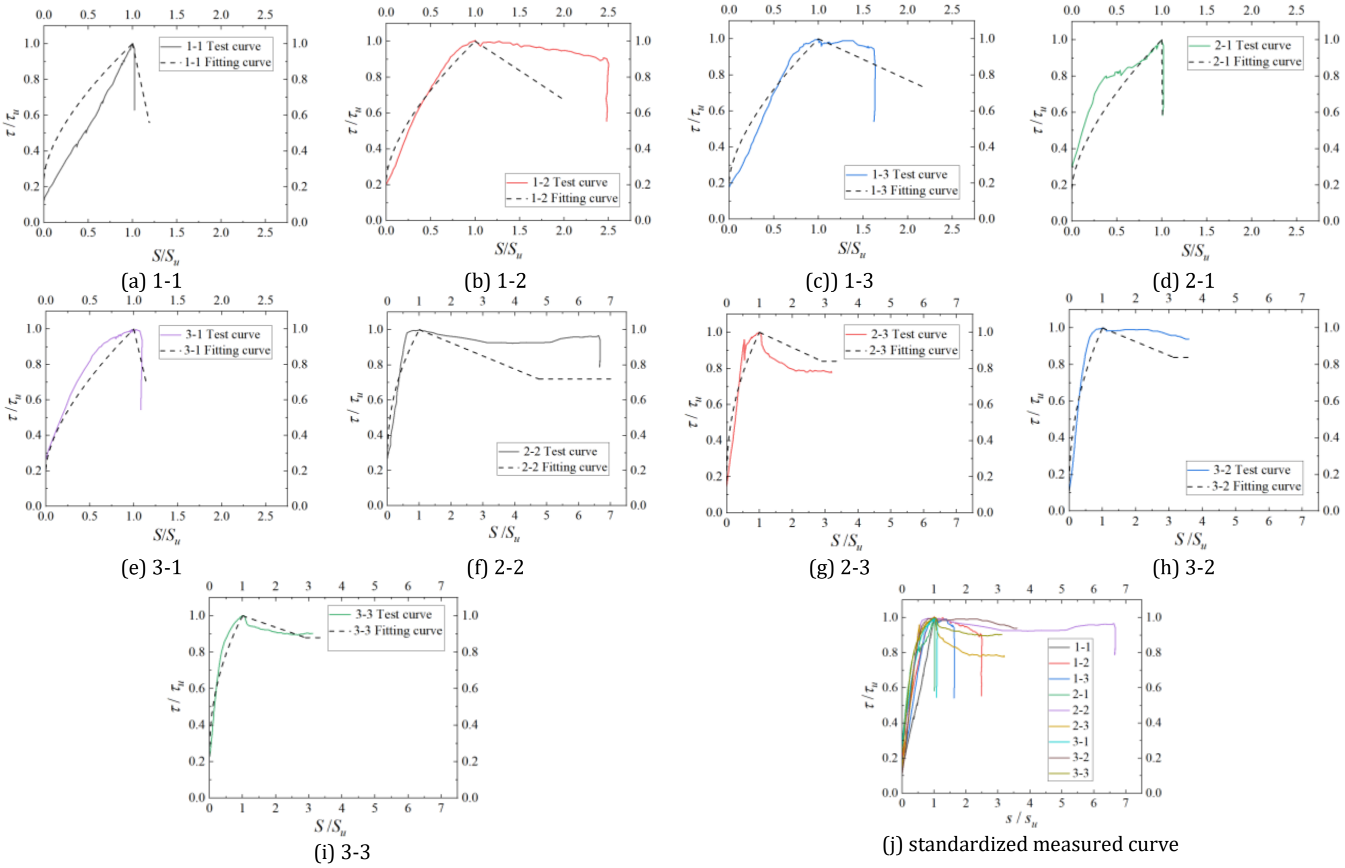

(a) 1-1 (b) 1-2 (c)) 1-3 (d) 2-1

(e) 3-1 (f) 2-2 (g) 2-3 (h) 3-2

(i) 3-3 (j) standardized measured curve

Fig. 12 Comparison of bonding stress-slip curves

Table 7. Comparison of characteristic bond strength and slip values

NO.	τ_0（MPa）		τ_u（MPa）		τ_r（MPa）		s_u（mm）		s_r（mm）	
	τ_{0c}	τ_{0t}	τ_{uc}	τ_{ut}	τ_{rc}	τ_{rt}	s_{uc}	s_{ut}	s_{rc}	s_{rt}
1-1	1.1	0.61	4.33	4.99	2.44	3.14	2.96	3.01	3.52	3.07
1-2	0.75	0.88	3.30	4.33	2.26	2.4	2.31	2.05	4.58	5.08
1-3	0.69	0.73	3.36	4.1	2.44	2.22	1.53	1.84	3.35	2.98
2-1	0.85	1.05	4.82	3.51	2.72	2.05	1.9	2.18	1.92	2.2
2-2	1.27	1.4	4.73	5.09	3.42	4.21	1.77	1.29	8.41	8.41
2-3	0.43	0.58	2.35	3.87	1.98	3	3.29	3.48	11.09	11.09
3-1	1.56	1.93	7.38	7.24	5.06	3.95	1.81	1.86	2.09	2.01
3-2	0.44	0.44	3.93	3.95	3.29	3.7	3.48	3.09	10.9	10.9
3-3	1.14	1.2	4.89	5.27	4.32	4.72	3.11	3.62	9.28	9.28
	$\overline{\tau_{0c}/\tau_{0t}}=0.98$		$\overline{\tau_{uc}/\tau_{ut}}=0.92$		$\overline{\tau_{rc}/\tau_{rt}}=0.97$		$\overline{s_{uc}/s_{ut}}=1.0$		$\overline{s_{rc}/s_{rt}}=1.0$	
	$\overline{\lvert\Delta\tau\rvert/\tau_{0t}}=0.20$		$\overline{\lvert\Delta\tau\rvert/\tau_{ut}}=0.16$		$\overline{\lvert\Delta\tau\rvert/\tau_{rt}}=0.19$		$\overline{\lvert\Delta s\rvert/s_{ut}}=0.13$		$\overline{\lvert\Delta s\rvert/s_{rt}}=0.06$	

The bond-slip constitutive relationship curves for each specimen can be plotted based on the calculated characteristic bonding strength and characteristic slip. The comparison between the standardized curves and the measured curves is shown on Fig.12.

Fig.12 demonstrates that the fitted curve of the bond-slip constitutive relationship between HPSFRC and H-shaped steel is in good agreement with the measured curve. The slope of the ascending segment of the curve for splitting failure specimen is slightly smaller than that for the push-out failure specimen, whereas the corresponding descending segment is relatively steeper. The descending segment of the curve for the push-out failure specimen is relatively gentle with a small slope which indicates that the bond stiffness of the specimen is higher than that of the split failure specimen. Push-out failure specimens exhibit ductile failure behavior, whereas splitting failure specimens undergo brittle failure. The relative values of the characteristic bonding strength and characteristic slip are presented in Table 8.

Table 8. Relative values of characteristic bonding strength and characteristic slip

No.	τ_{0c}/τ_{uc}	τ_{rc}/τ_{uc}	τ_{0t}/τ_{ut}	τ_{rt}/τ_{ut}	s_{rc}/s_{uc}	s_{rt}/s_{ut}
1-1	0.25	0.56	0.12	0.63	1.19	1.02
1-2	0.23	0.68	0.2	0.55	1.98	2.48
1-3	0.21	0.73	0.18	0.54	2.19	1.62
2-1	0.18	0.56	0.3	0.58	1.01	1.1
2-2	0.27	0.72	0.28	0.83	4.75	6.52
2-3	0.18	0.84	0.15	0.78	3.37	3.19
3-1	0.21	0.68	0.27	0.55	1.15	1.08
3-2	0.11	0.84	0.11	0.94	3.13	3.53
3-3	0.23	0.88	0.23	0.90	2.98	2.56

For splitting failure specimens, the ratio of measured residual bond strength to ultimate bond strength ranges from a minimum of 54.1% to a maximum of 62.9%. In contrast, this ratio for push-out failure specimens falls within the range of 78% to 94%. For splitting failure specimens, the measured residual slip to peak slip ranges from 1.02 to 2.48, in contrast, this ratio for push-out failure specimens falls within the range of 2.56 to 6.52. By comparison, splitting failure specimens experience a more substantial reduction in bearing capacity and exhibit smaller relative slip upon failure. In contrast, push-out failure specimens undergo a negligible decline in bearing capacity while developing considerably larger relative slip.

5. Conclusions

The bond performance between welded H-shaped steel and HPSFRC was studied through the push-out test. Four influencing factors were mainly considered including concrete strength, concrete cover thickness, anchorage length and stirrup ratio. Based on the load-slip data at the loading end and observed test phenomena, the types of bonding failure, the fitting expressions of characteristic bond strength and characteristic slip, as well as the related influencing factors were analyzed, and the bond-slip constitutive relationship was proposed. On the basis of the test results, the main conclusions are drawn as follows.

The specimens experienced two failure modes: splitting failure and push-out failure. The equivalent constraint coefficient r_e was proposed. Splitting failure occurred when r_e was not greater than 4.41%. Push-out failure occurs when r_e was greater than 4.41%. This classification criterion was verified using relevant test results.

When the specimens failed, two crack configurations were identified at the end: linear and oblique forms. The transverse expansion deformation of H-shaped steel under compressive loading exerts compressive stress on the interfacial concrete, which subsequently induces crack initiation at the weak positions of the concrete. Owing to the bonding and bridging effects between steel fibers and concrete, increasing the volume percentage of steel fibers can effectively inhibit the initiation and propagation of cracks.

Increasing the concrete cover thickness and the volume percentage of steel fibers can enhance the ultimate bond strength, while extending the anchorage length tends to reduce the ultimate bond strength. Increasing the stirrup ratio has little effect on the ultimate bond strength for HPSFRC specimens containing stirrups.

Considering the comprehensive influencing factors, the expression for the characteristic bond strength between H-shaped steel and HPSFRC was fitted using both the data from this experiment and the experimental data reported by other scholars. Verification results confirm that the predicted values of the characteristic bonding strength are in good agreement with the measured values, with all correlation coefficients exceeding 0.8.

The characteristic slip expression was obtained through data fitting, and the bond-slip constitutive relationship models were established separately for splitting failure and push-out failure. The splitting failure model adopts a three-segment linear form, whereas the push-out failure model follows a four-segment linear form.

The established bond-slip constitutive relationship was based on the average bond stress and the slip at the loading end, while the local bond stress slip constitutive relationship was not investigated. The establishment of local bond stress slip constitutive relationship relies on the acquisition of more accurate experimental data. The volume percentage of steel fibers, the concrete cover thickness, the anchorage length and the stirrup ratio exert a combined influence on the bond strength. Nevertheless, the optimal values and applicable ranges of each parameter require further investigation for clarification.

Acknowledgement

The authors wish to acknowledge the Henan Provincial Science and Technology Research Project, China (Grant No. 252102240022 and GZS2022013).

Reference

Cao, X., Xie, X. D., Zhang,T. Y., Du,G. F. 2023. Bond-slip behavior between high-strength steel tube and Ultra-high-Performance Concrete. Structures. 47, 1498-1510. https://doi.org/10.1016/j.istruc.2022.11.052

Huang, H., Gao, X., Li, L, Wang, H. 2018. Improvement effect of steel fiber orientaition control on mechanical performance of UHPC. Constr. Build. Mater. 188, 709-721. https://doi.org/10.1061/j.conbuildmat.2018.08.146.

Huang, Z. Y., Huang, X. X., Li, W. W., Chen, C. F., Li, Y. J., Lin, Z. W., Liao, W. 2021. Bond-slip behaviour of H-shaped steel embedded in UHPFRC. Steel and Composite Structures. 38(5): 000-000. https://doi.org/10.12989/scs.2021.38.5.000

Huang, Z. Y., Lin, G., Huang, X. X., Li, W., Sui, L. L., Youtam. 2024. Bond-slip constitutive model and numerical simulation of shaped steel embedded in UHPC. Industrial Construction. 54 (3): 143-152. https://doi.org/10.13204/j.gyjzG21092803

Jiang, G. V., Wu, M. Q., Li, S. S. 2022. Bond-slip model of steel ultra-high performance concrete interface. Shanghai Building Materials. (6) :20-25. https://doi.org/10.3969/j.issn.1006-1177.2022.06.004

Jin, L. B., Duan, J., Wu, Q., Zhou, P. Jiao, P. F., Dong, T. Y. 2023. Review on mix ratio design of high-performance concrete. Concrete. 403, 168-174. https://doi.org/10.3969/j.issn.1002-3550.2023.05.034

Kim, D. J., Park, S. H., Ryu, G. S., Koh, K.T. 2011. Comparative flexural behavior of hybrid ultra high-performance fiber reinforced concrete with different macro fibers. Construction and Building Materials, 25(11): 4144–55. https://doi.org/10.1016/j.conbuildmat.2011.04.051.

Li, Y. Y., Li, X. Q., Su, H. B. 2017. Experimental analysis of bond-anchorage properties between 600 MPa high strength reinforcement and concrete. Journal of Civil and Environmental Engineering. 39(2):20-25. https://doi.org/10.11835/j.issn.1674-4764.2017.02.003

Liang, R., Huang, Y. 2024. Experimental study on bond splitting strength ultra-high-performance concrete with steel bars. Journal of Building Structures. (6): 254-261. https://doi.org/10.14006/j.jzjgxb.2022.0720

Liu, L. J., Wang, J. C., Huang, B., Xv, X. Y. 2025. Application process of close packing theory in concrete mix design. Concrete. 425, 20-23. https://doi.org/10.3969/j.issn.1002-3550.2025.03.004

Liu, Z. Q., Ren, B. Y., Xue, J. Y. 2023. Experimental study and finite element analysis on flexural performance of high-strength steel reinforced ultra-high performance concrete beam. 40(4): 102-114. https://doi.org/10.6052/j.issn.1000-4750.2021.10.0765

Ming, M., Zheng, S. S., Yang, S., Xu, Y. H., Song, M. C. 2022. Experimental study on the constitutive relationship between shaped steel and HPFRC. Structures. (38): 76-93. https://doi.org/10.1016/j.istruc.2022.01.043

Ming, M., Zheng, S. S., Zhang, Y. X., Zheng, Y., Yang, S., Song, M. C. 2021. Experimental study on the bond-slip behavior and stress transfer mechanism between shaped steel and high-performance fiber-reinforced concrete. Structures. 34: 5013-5028. https://doi.org/10.1016/j.istruc.2021.09.014

Roeder, C. W., Chmielowski, R., Brown, C. B. 1999. Shear connector requirements for embedded steel sections. Journal of Structural Engineering. 125: 142-151. https://doi.org/10.1061/(ASCE)0733-9445(1999)125:2(142)

Shi, G., Shao, X. D., Gao, L. Q., Cao, J. H., Chen, L. J. 2021. Experimental research on bond performance between HRB400 rebar and ultra-high-performance concrete. Bridge Construction. 51(6): 61-67. https://doi.org/10.3969/j.issn.1003-4722.2021.06.009

Tűrker, K., Yavas, A., Birol, T., Gűltekin C. 2021. Evaluation of using ultra-high performance fiber reinforced concrete in I-section RC beam. Journal of the Faculty of Engineering Architecture of Gazi University. 36(3): 1431–48. https://doi.org/10.17341/gazimmfd.803936.

Voo, Y. L., Foster, S. J. 2010. Characteristics of ultra-high performance ductile concrete and its impact on sustainable construction. The IES Journal Part A. 3(3):168–87. https://doi.org/10.1080/19373260.2010.492588.

Wang, R. L., Ma, B. 2018. Experimental study on Bonding and Anchoring of Reinforcing Bars and Ultra-High-Performance Concrete. Urban Roads Bridges & Flood Control. (9): 204-207. https://doi.org/10.16799/cnki.csdqyfh.2018.09.056

Wang, L. F., Wang, K., Zhang, M., Yang, Y., Liu, F. C., Yang, D. D., Xu, G. P., Chen, W. H. 2023. Seismic performance of steel-reinforced reactive powder concrete columns. Structures. 54: 1788-1802. https://doi.org/10.1016/j.istruc.2023.05.100

Xu, K. C., Qin, T. L., Huang, L. J., Zhang, L. Q., Yao, F., Han, B. G. 2024. Experimental study of interfacial bonding performance between section steel and ultra high-performance concrete. Journal of Construction Steel Research. 213, 108347. https://doi.org/10.1061/j.jcsr.2023.108347.

Yavas, A., Ince, M. 2021. Effect of reinforcement ratio on flexural behavior of I-shaped UHPFRC beams.Structures. 34: 4457-4465. https://doi.org/10.1016/j.istruc.2021.10.051.

Yazdan, M., Cheng-Tzu, T. H., Sun, P. 2014. Local bond–slip behavior between cold-formed metal and concrete. Engineering Structures. 69, 271-284. https://doi.org/10.1016/j.istruc.2022.01.043

Yu, X. M., Liu, Z. W., Ruan, Y. M., Qin, C. C., Wang D. H., Ju., Y. Z. 2022. Bond behavior between ultra-high-performance concrete (uhpc) and steel bar with different strengths. Strength of materials. 54(6): 1138-1144. https://doi.org/10.1007/s11223-023-00488-6

Zhang, J. R., Meng, X. Y., Song, J. X., Cao, X. W., Ma, K. Z. 2023. Push-out tests of interfacial bond slip between H-shaped steel and ultra-high-performance concrete. Structures. 57, 105268. https://doi.org/10.1061/j.istruc.2023.105268.

Zhang, L. F., Wang, K., Ling, Z. B., Ahmad. A. O., Guo, K. 2023. Bond-slip behavior between reactive powder concrete and H-shaped steel. Journal of Construction Steel Research. 210, 108058. https://doi.org/10.1016/j.jcsr.2023.108058

Zhao, C. H., Li, H. D., Deng, K. L. 2019. Experimental study on bonding performance between rebar and coarse aggregate ultra-high-performance concrete. 54(5): 938-943. https://doi.org/10.3969/j.issn.0258-2724.20170513

Zhao, X. D., Shao, X. D., Cao, J. H., Shao, Z. X., Ying-li, R. J. 2022. Experimental studies on shear behavior of the UHPC composite beam with hot rolled shaped steel. Engineering Structures. 274, 115160. https://doi.org/10.1016/j.engstruct.2022.115160

Wang, K., Wei, L., Zhu, Y. Z., Zhu, Z. Y., Hou, X. M., Luo, H. H., Wang, J. H., Chen. Z. X. 2025. Experimental study and analysis on the flexural behavior of steel hollow section reinforced UHPC beams. Thin-Walled Structures. 217, 113762. https://doi.org/10.1016/j.tws.2025.113762

Disclaimer